Analytical and Bioanalytical Chemistry (2022) 414:7277–7289
https://doi.org/10.1007/s00216-022-04279-x

RESEARCH PAPER

Homogeneous photoelectrochemical biosensor for sensitive detection of omethoate via ALP-mediated pesticide assay and Bi_2S_3@$Bi_2Sn_2O_7$ heterojunction as photoactive material

Min Wang[1] · Li Hou[1] · Xiaoyu Chen[1] · Tianran Lin[1]

Received: 4 July 2022 / Revised: 1 August 2022 / Accepted: 9 August 2022 / Published online: 19 August 2022

Abstract

A simple homogeneous photoelectrochemical (PEC) sensing platform based on an alkaline phosphatase (ALP)–mediated pesticide assay was established for the sensitive detection of omethoate (OM). The Bi_2S_3@$Bi_2Sn_2O_7$ heterojunction was used as a photoactive material to provide stable background photocurrent signals. The inhibition of OM on ALP and PEC determination was carried out in the homogeneous system. In the absence of OM, dephosphorylation of L-ascorbic acid 2-phosphate trisodium salt (AAP) was catalyzed by ALP to produce the enzyme-catalyzed product (L-ascorbic acid, AA). AA, as an electron donor, could capture photogenerated holes on the Bi_2S_3@$Bi_2Sn_2O_7$ heterojunction, thus inhibiting the recombination of electron holes to achieve an increase of the photocurrent signal. When the OM was introduced, the enzyme activity of ALP was reduced due to the organophosphorus pesticides (OPs)–based enzyme inhibition, and the AA produced by catalytic hydrolysis was also reduced, thus reducing the photocurrent signal. Compared with the traditional PEC sensor for OPs, this homogeneous PEC sensor avoided immobilization procedures, covalent labeling, separation, and the steric hindrance effect caused by immobilized biomolecules, which achieved high recognition efficiency and caused a reduction in analysis time. Additionally, an ALP-mediated pesticide assay for the determination of OPs with a simplified experimental process further improved the stability and reproducibility of the PEC sensor. The PEC sensor showed high sensitivity to the target OM within a dynamic range of 0.05 ~ 500 ng mL^{-1}, and the detection limit was 0.0146 ng mL^{-1}. Additionally, the PEC biosensing system showed good selectivity and anti-interference ability, and exhibited a satisfactory result in spinach and mustard samples.

Keywords Photoelectrochemical sensor · Omethoate · Electron donor · Homogeneous biosensor

Introduction

Pesticides have been widely used worldwide for their efficient control of insects and pests in agriculture, as well as ensuring crop quality and yield. Among them, organophosphorus pesticides (OPs), as the most widely used pesticides, are favored by people because of their high pest control effect and low persistence. However, the overuse or improper handling of OPs can cause some serious public health problems and cause serious harm to soil, water, atmosphere, fruits, and vegetables and other non-target organisms (such as birds and fish), which in turn poses a huge threat to human health through the food chain [1–3]. OPs can combine with acetylcholinesterase (AChE), so that the activity of AChE is irreversibly inhibited and destroyed the nervous system of humans, leading to choline poisoning and even death. Consequently, much effort needs to be paid to explore effective and sensitive detection methods for OPs.

Photoelectrochemical (PEC) method has undergone rapid development and attracts wide attention since it perfectly inherits the advantages of optical analysis and electrochemical sensors. The detection signal (photocurrent) is completely separated from the excitation light source (mostly xenon lamp); therefore, the PEC biosensor has low background noise and ultra-high sensitivity [4]. PEC analysis method is mainly based on using

✉ Li Hou
houli@mailbox.gxnu.edu.cn

✉ Tianran Lin
tianranlin@163.com

[1] School of Chemistry and Pharmaceutical Sciences, State Key Laboratory for Chemistry and Molecular Engineering of Medicinal Resources, Guangxi Normal University, Guilin 541004, People's Republic of China

photoactive electrode as transducer, and generating measurable current signal through photoinduced electron–hole pairs separation, thus indirectly achieving the analysis and detection of the target [5, 6]. Fundamentally, the photocurrent response of the PEC biosensor largely depends on the photoactive materials, which are used to construct the photoelectrode. However, the process of fixing the recognition element (aptamer, antibody, peptide and enzyme) on photoactive materials beforehand is complicated and time-consuming and the recognition element is easily loose, which affects the reproducibility and stability of the biosensors [7, 8]. Moreover, the configurational freedom of the immobilized recognition element is usually restricted and produces the steric hindrance effect, which makes the low recognition efficiency and causes the enhancement of analysis time. Therefore, it is urgent to design a new signal transduction mode to improve the performance of the PEC biosensor.

To address the above problems, it is highly preferable to develop a homogeneous PEC biosensor by abandoning such immobilization procedures, covalent labeling, separation, and conducting both target recognition and signal amplification in homogeneous solutions [9]. What's more, this method not only avoids the destruction of biomolecules during PEC detection, but also avoids the steric hindrance effect caused by immobilized biomolecules, thus achieving highly sensitive and accurate detection of target analytes with simple sensing operations [10]. Therefore, homogeneous photoelectrochemical sensor can be emerged as a powerful and promising tool for the detection of OPs in actual samples. Among the currently established sensor assays for the detection of OPs, most articles are based on AChE-mediated pesticide assay [11–13]. However, preliminary work of our group has found that the stability of alkaline phosphatase (ALP)–based pesticide assay is superior to the AChE-based pesticide assay. It is because of the fact that AChE is highly susceptible to inactivation. ALP is widely used in biosensors because of its high catalytic activity, broad substrate specificity, and mild reaction conditions as well as good stability [14]. Zhang's research group constructed an ALP-regulated UiO-66-NH_2/MnO_2 fluorescence probe for total OPs determination, establishing a relationship between OPs level and fluorescence intensity by the reaction product AA [15]. Cai and co-workers [16] used ALP and self-assembled MnO_2-AuNCs-SiO_2 to construct a fluorescence-colorimetric sensor for OPs detection in which the product AA can decompose MnO_2 and restore fluorescence. The catalytic activity of ALP is inhibited because OPs and the amino acid residues of ALP such as Gln375, Asp55, and Thr413 will form hydrogen bonds [17]. The known ALP-based pesticide assay for the PEC determination of OPs was rarely reported so far.

The exploration of photoactive materials with high photoelectric conversion efficiency is of significant importance for establishing high-performance PEC sensors. Bismuth sulfide, as an orthocrystalline n-type semiconductor, has an adjustable band gap between 1.3 eV and 1.7 eV, diversified morphology, and simple synthesis technology. It is easy to be excited to generate electron–hole pairs under visible light, and shows a strong light absorption ability in the visible region. Due to its good stability, non-toxicity, simple synthesis method, cost-effectiveness, and good photoelectric performance, it has been widely concerned in the field of PEC sensing and biosensing. Unfortunately, pure Bi_2S_3 nanomaterials have a high photoelectron-hole pair binding rate, low photoelectric conversion efficiency, and fewer carriers for surface reaction, resulting in low PEC response and thus limiting its practical application. Normally, the construction of semiconductor/semiconductor heterojunction can greatly inhibit the recombination rate of electron–hole pairs, increase the lifetime of the carrier, and thus improve the photoelectric conversion efficiency to increase the photocurrent signal [18]. Considering that the narrow band gap of $Bi_2Sn_2O_7$ and Bi_2S_3 with a good energy level matching relationship can form a high-performance n-p type Bi_2S_3@$Bi_2Sn_2O_7$ heterojunction. The Bi_2S_3@$Bi_2Sn_2O_7$ heterojunction has strong visible-light absorption properties, which can accelerate the separation efficiency of photogenerated electron–hole pairs, improving the photoelectric conversion efficiency, and generating a stable background photocurrent signal [19]. To the best of our knowledge, there is no report focusing on ALP-based pesticide assay for the homogeneous PEC determination of OPs by coupling with the Bi_2S_3/$Bi_2Sn_2O_7$ as photoactive material.

Inspired by the above issues, this work designed a label-free, homogeneous PEC biosensor based on the ALP enzyme inhibition strategy for OPs (omethoate as a model, OM) detection. In the experimental process, there was no need for complex experimental equipment and tedious electrode cleaning steps compared with the traditional electrochemical sensor construction process. The electrode was free of any biomolecular modification, because biomolecules are extremely unstable and prone to inactivation during the light irradiation of PEC measurement. As depicted in Scheme 1, Bi_2S_3@$Bi_2Sn_2O_7$ heterojunction was used as the photoactive substrate material to generate stable photocurrent signals. The enzymatic activity inhibition process was carried out in a homogeneous solution to avoid false positive signals due to steric hinders caused by alkaline phosphatase (ALP), and L-ascorbic acid 2-phosphate trisodium salt (AAP) is catalyzed by ALP to generate the enzyme-catalyzed product (L-ascorbic acid, AA). AA as a commonly used electron donor for PEC sensing can effectively inhibit the recombination of photogenerated electron–hole pairs in the Bi_2S_3@Bi_2Sn_2O7 heterojunction and improve the photoelectric conversion efficiency, thereby increasing the photocurrent, which plays a significant role in signal amplification. In the presence of OM, the enzyme activity of ALP is reduced based on the enzymatic inhibition of ALP by OPs, so that

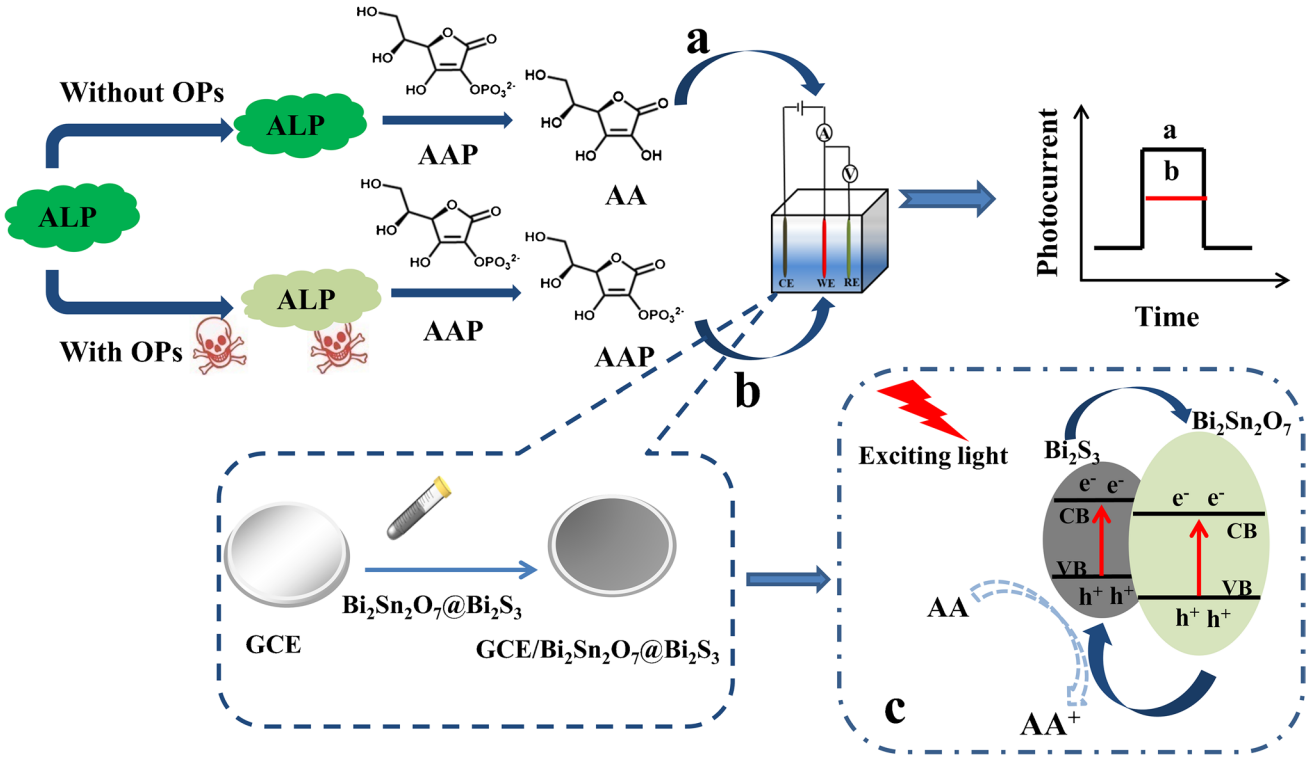

Scheme 1 The schematic illustration of the sensing system based on the $Bi_2S_3@Bi_2Sn_2O_7$ heterojunction for OM determination

the production of AA by catalytic hydrolysis is also reduced, resulting in a decrease in the measured photocurrent signal. Based on the relationship between the inhibition of OM and the photocurrent response, a homogeneous PEC sensor was constructed for the rapid and sensitive detection of OM, which results in satisfactory repeatability and stability. At the same time, the PEC sensor not only has good accuracy and stability, but also has a broad application prospect in the actual spinach and mustard samples, and provides an alternative PEC strategy for the general detection of other OPs.

Experimental section

Reagents and materials

Tin(IV) chloride pentahydrate ($SnCl_4{\cdot}5H_2O$, 99.0%), ascorbic acid (AA, 99.0%), disodium hydrogen phosphate (Na_2HPO_4, 99.0%), and potassium dihydrogen phosphate (KH_2PO_4, 99.0%) were purchased from Aladdin Reagent Co., Ltd. (Shanghai, China). Omethoate, methyl parathion, monocrotophos, phorate, triazophos, paraquat, thiamethoxam, acetochlor, and tebuconazole standard solution (100 μg mL^{-1}) were purchased from Tanmo Quality Inspection Standard Substance Center (Beijing, China). Glycol, potassium ferricyanide ($K_3[Fe(CN)_6]$, 99.0%), and potassium ferrocyanide ($K_4[Fe(CN)_6]$, 99.0%) were purchased from Xilong Scientific Co., Ltd. (Guangdong, China). Bismuth nitrate ($Bi(NO_3)_3{\cdot}5H_2O$, 99.0%) and urea (99.0%) were obtained from Chengdu Cologne Chemical Co., Ltd. (Sichuan, China). Sodium sulfide ($Na_2S{\cdot}9H_2O$, 98.0%) was purchased from Macklin Biochemical Technology. Co., Ltd. (Shanghai, China). Alkaline phosphatase (ALP) was purchased from Sigma Corporation (USA). L-ascorbate-2-sodium phosphate (AAP, 95%) was purchased from Yuanye Biotechnology Co., Ltd. (Shanghai, China). All the chemicals used in the experiment were analytical grade and used directly without further purification. The ultrapure water (≥ 18.2 MΩ cm) was purified by a Milli-Q water purifying system (Milli-Q, Millipore, USA).

Instruments and apparatus

The morphology of the nanomaterials was characterized and analyzed by transmission electron microscope (TEM) and high-resolution transmission electron microscope (HR-TEM) (Thermo Fisher Scientific, USA). X-ray photoelectron spectroscopy (XPS) was obtained from the instrument model ESCALAB 250Xi (Thermo Fisher Scientific, USA). X-ray powder diffraction (XRD) was measured on D/max-3c (Rigaku, Japan). Raman spectra were obtained by Renishaw inVia (Renishaw company, UK) which was excited by a 514 nm laser. Fourier transform infrared spectroscopy (FT-IR) spectra were monitored by a FT-IR spectrometer

(Spectrum Two, PerkinElmer, USA). Using barium sulfate as reference material, the vis diffuse reflectance (UV–vis DRS) spectrum was studied with a UV-2600 UV–vis spectrophotometer (Shimadzu, Japan). High-performance liquid chromatography was tested on an LC-20AT chromatograph (Shimadzu, Japan), and the chromatographic column was a C18 column (250 × 4.6 mm, 5 μm) (GL Sciences, Japan).

The electrochemical impedance spectroscopy (EIS) and cyclic voltammetry (CV) in the electrochemical test were measured by the RST5200F electrochemical workstation (Zhengzhou Shiruisi Instrument Technology Co., Ltd., China). The experimental operating conditions of EIS are as follows: the test was carried out in a $[Fe(CN)_6]^{3-/4-}$ (containing KCl) solution with a frequency of 0.01–10^5 Hz and an amplitude of 50 mV. The experimental operating conditions of CV are as follows: the test was carried out in $Fe(CN)_6]^{3-/4-}$ (containing KCl) solution with a voltage range of − 0.2–0.6 V and a scan rate of 50 mv s^{-1}. The photoelectrochemical test device was built by connecting a 500 W xenon lamp light source (Beijing Newbit Instrument Co., Ltd., China) with the electrochemical workstation to record the photoelectric signal. All PEC experiments were carried out in a self-made three-electrode system with a glassy carbon electrode (GCE, $\Phi = 3$ mm) as the working electrode, platinum wire electrode as the counter electrode, and Ag/AgCl (saturated KCl) as the reference electrode.

Preparation of photoactive materials

According to the previously reported method [20], Bi_2S_3 nanorods were synthesized by a one-step hydrothermal method. Firstly, 1.83 g of $Bi(NO_3)_3{\cdot}5H_2O$ was dispersed in 25 mL ethylene glycol, and solution A was obtained by magnetic stirring for 20 min. At the same time, 1.35 g of $Na_2S{\cdot}9H_2O$ was added into the 30 mL water for magnetic stirring for 15 min to obtain solution B. Then, 1.92 g urea was ultrasonically dispersed in 20 mL of water to obtain solution C. Solution B was quickly added to solution A to obtain a large amount of black suspension with an irritating smell. After that, solution C was mixed with the above solution and ultrasonically dispersed for 20 min to obtain the mixed solution. The obtained black suspension was heated in a 100 mL Teflon-lined autoclave and kept at 180 ℃ for 24 h. After the reaction was accomplished, the product was cooled naturally to room temperature, and then washed with ultrapure water and ethanol for three times, respectively. Then, the product Bi_2S_3 was obtained by vacuum drying at 60 ℃ for 6 h.

The synthesis of $Bi_2Sn_2O_7$ was as follows [21]: firstly, 0.90 g of $SnCl_4{\cdot}5H_20$ was dissolved in 20 mL ultrapure water, and it was completely dissolved by magnetic stirring at room temperature for 25 min. Then, the pH of the above solution was adjusted to 6 with 4 mol L^{-1} of NaOH solution, during which a large amount of milky white precipitate was rapidly produced. After that, the precipitate was obtained by centrifugation at 5000 rpm for 5 min. The white precipitate and 1.95 g of $Bi(NO_3)_3{\cdot}5H_2O$ were completely dispersed in 40 mL water by strong stirring for 20 min. The pH of the white suspension was adjusted to 12 with NaOH solution and dispersed ultrasonic for 20 min. Then, it was transferred into a Teflon-lined autoclave and kept at 180 ℃ for 24 h. Finally, the white powder of $Bi_2Sn_2O_7$ was collected by centrifugation, washed with ultrapure water for several times, and then vacuum dried at 60 ℃ for 8 h.

$Bi_2S_3@Bi_2Sn_2O_7$ nanocomposites with different Bi_2S_3 contents were prepared by a simple physical adsorption method. The specific operation of the experiment was as follows: the above-prepared $Bi_2Sn_2O_7$ and Bi_2S_3 were mixed and dispersed in a certain proportion. Then, the heterojunctions were obtained by sonication at 28 °C for 30 min in ethanol solution.

Fabrication of the PEC sensing interface

Before the electrode modification, the glassy carbon electrode (GCE) was first polished with 0.05 μm alumina powder on the chamois, polished to a mirror surface, rinsed with ultrapure water, and then ultrasonicated with ethanol and ultrapure water. Wash it for 1 min and dry it at room temperature for later use. Nine microliters of the prepared $Bi_2S_3@Bi_2Sn_2O_7$ nanohybrid material and 3 μL of Nafin/ethanol solution (v/v, 1%) were drop-coated onto the polished clean GCE ($\Phi = 3$ mm). After that, the modified electrode was naturally dried at room temperature for 30 min to form a uniform and stable film.

PEC detection of OM

25 μL of OM standards or samples with diverse concentrations and 5 μL of 2000 U L^{-1} ALP solution were added to 70 μL of PBS (10 mmol L^{-1}, pH 7.4) buffer solution and incubated at 37 ℃ for 30 min. Subsequently, 50 μL of 100 mmol L^{-1} AAP solution and 50 μL of PBS (10 mmol L^{-1}, pH 7.4) buffer solution were added and incubated at 37 ℃ for 30 min to obtain a solution of OM-inhibited enzyme-catalyzed product. The enzyme-catalyzed product (ascorbic acid, AA) was transferred to a PEC detection cell containing a certain volume of PBS (10 mmol L^{-1}, pH 7.4) solution, and the prepared $Bi_2S_3@Bi_2Sn_2O_7$ heterojunction photoelectrode was immersed into the PEC detection cell for PEC determination. A 500 W xenon lamp was used as the light source, the lamp switching interval was 20 s, and the applied potential was 0.2 V. All experiments were carried out at room temperature.

Sample preparation and extraction

Two kinds of vegetable samples such as spinach and mustard were purchased from a local farmers' market. The pretreatment method was as follows: 2 g of spinach and mustard

was weighed and mashed into centrifuge tubes, and 20 mL of methanol solution was added to each tube, for ultrasonic treatment for 30 min at room temperature, followed by centrifuging at 10,000 rpm for 10 min, and filtering the supernatant with a 0.2 μm filter and diluting it 5 times as the control samples. In addition, different volumes of OM standard solutions were spiked into the above-mentioned vegetable samples via the same sample treatment process, respectively. The spiked samples with OM concentrations were 0.5, 5, and 10 μg mL^{-1}, respectively. The HPLC experimental conditions were as follows: the injection volume was 20 μL, the detection wavelength was 210 nm, the total flow rate was 1.0 mL min^{-1}, and the mobile phase was V (acetonitrile):V (water) = 10:90. The peak area external standard method was used for quantification. Then, the sample solutions containing 0.5, 5, and 10 μg mL^{-1} were diluted with PBS buffer (10 mmol L^{-1}, pH 7.4) to 0.05, 50, and 500 ng mL^{-1}, respectively, and the constructed PEC biosensor was used for detection.

Storage stability test

The enzyme-catalyzed product solution (electron donor, AA) produced from the OPs-based enzyme inhibition assay was transferred to a PEC detection cell, and the prepared Bi_2S_3@$Bi_2Sn_2O_7$ heterojunction photoelectrodes were immersed into the PEC detection cell for PEC determination. After each measurement, the modified electrodes were washed with ultrapure water and kept in the refrigerator at 4 ℃ to avoid light until the next period of measurement; the experimental procedure was repeated for measurement every 3 days.

Results and discussion

Characterization of Bi_2S_3@$Bi_2Sn_2O_7$ nanomaterials

To prove the successful preparation of the photoactive material, the morphologies of $Bi_2Sn_2O_7$, Bi_2S_3, and Bi_2S_3@$Bi_2Sn_2O_7$ heterojunctions were characterized by TEM and HTEM. As shown in Fig. 1A and 1B, it can be seen that Bi_2S_3 has a nanorod-like structure with an average diameter and length of about 10 nm and 100 nm, and $Bi_2Sn_2O_7$ aggregates between nanoparticles of about 15 nm; the mutual aggregation of the nanoparticles is conducive to absorbing visible light to some extent [22]. The TEM and HR-TEM images of Bi_2S_3@$Bi_2Sn_2O_7$ heterojunction material are shown in Fig. 1C and Fig. S1A; it can be clearly seen that many spherical nanoparticles with uniform size are attached to the surface of Bi_2S_3 nanorods. As displayed in Fig. S1B and inset, the interplanar spacing is about 0.318 nm and 0.287 nm, corresponding to the (222) plane of $Bi_2Sn_2O_7$ and the (211) plane of Bi_2S_3 [23, 24], which all prove the formation of composites between Bi_2S_3 and $Bi_2Sn_2O_7$. In order to further explore the distribution of $Bi_2Sn_2O_7$ nanoparticles on the surface of Bi_2S_3 nanorods, Fig. S1C and Fig. 1D are the EDS spectra and elemental mapping of Bi_2S_3@$Bi_2Sn_2O_7$ heterojunctions, from which it can be seen that Bi, O, S, and Sn elements are uniformly distributed, which also proves the uniform growth of $Bi_2Sn_2O_7$ nanoparticles on Bi_2S_3 nanorods.

The corresponding Fourier transform infrared spectra (FT-IR) of different materials are presented in Fig. 1E. In cure of $Bi_2Sn_2O_7$, the peaks near 556 cm^{-1} and 617 cm^{-1} correspond to the stretching vibrations of Bi-O and Sn–O, respectively [25]. Bi_2S_3 has a peak value at 844 cm^{-1}, corresponding to the o Bi-S vibration [26]. Meanwhile, Fig. 1F shows the Raman spectra of Bi_2S_3, $Bi_2Sn_2O_7$, and Bi_2S_3@$Bi_2Sn_2O_7$ heterojunctions. The main peaks of Bi_2S_3 are 136 cm^{-1}, 186 cm^{-1}, 236 cm^{-1}, and 256 cm^{-1}, which are consistent with the reports in the literature [27]. In the $Bi_2Sn_2O_7$ spectrum, 248 cm^{-1} and 382 cm^{-1} are mainly the Eg and F2g stretching modes of Bi-O, and 400 cm^{-1} is the F2g stretching mode of Sn–O [28]. The characteristic peaks of Bi_2S_3 and $Bi_2Sn_2O_7$ can also be obviously observed in Bi_2S_3@$Bi_2Sn_2O_7$ heterojunction, which is sufficient to prove the successful preparation of the heterojunction composite material. Next, the crystallization and purity of the material are explained by the XRD spectrum as shown in Fig. 1G. It can be seen from the figure that the diffraction peak position of Bi_2S_3 is almost consistent with the standard card (JCPDSNo.17–0320) [29]. The main peak position of $Bi_2Sn_2O_7$ was almost exactly the same as that of the standard card (JCPDSNo.87–0284) [30], as can be seen from the spectrum that a few miscellaneous peaks are generated, which may be caused by the formation of other crystals due to the high local temperature in the reaction kettle during the synthesis of $Bi_2Sn_2O_7$ at high temperature [31]. In addition, these peaks also reflect the overall crystallinity of the material is better. The main diffraction peaks of Bi_2S_3 and $Bi_2Sn_2O_7$ can also be seen from the spectrogram of Bi_2S_3@ $Bi_2Sn_2O_7$ heterojunction, which proves the successful preparation of the photoactive material. In order to further determine the composition of Bi_2S_3@$Bi_2Sn_2O_7$ heterojunction, XPS spectra were used to analyze the chemical composition and valence states of chemical elements on the material surface. Figure 1H shows the full spectrum of Bi_2S_3@$Bi_2Sn_2O_7$; the heterojunction mainly contains elements Bi, S, C, O, and Sn. The C element may be the carbon band sample of the XPS instrument itself, which is used to calibrate the instrument, indicating that the prepared heterojunction material is pure and does not contain other elements. As displayed in Fig. S2, the high-resolution spectra of Bi 4f, S 2p, Sn 3d, and O 1 s are respectively shown, from which it is observed that the characteristic peaks of Bi 4f are at Bi $4f_{7/2}$ (157.3 eV,

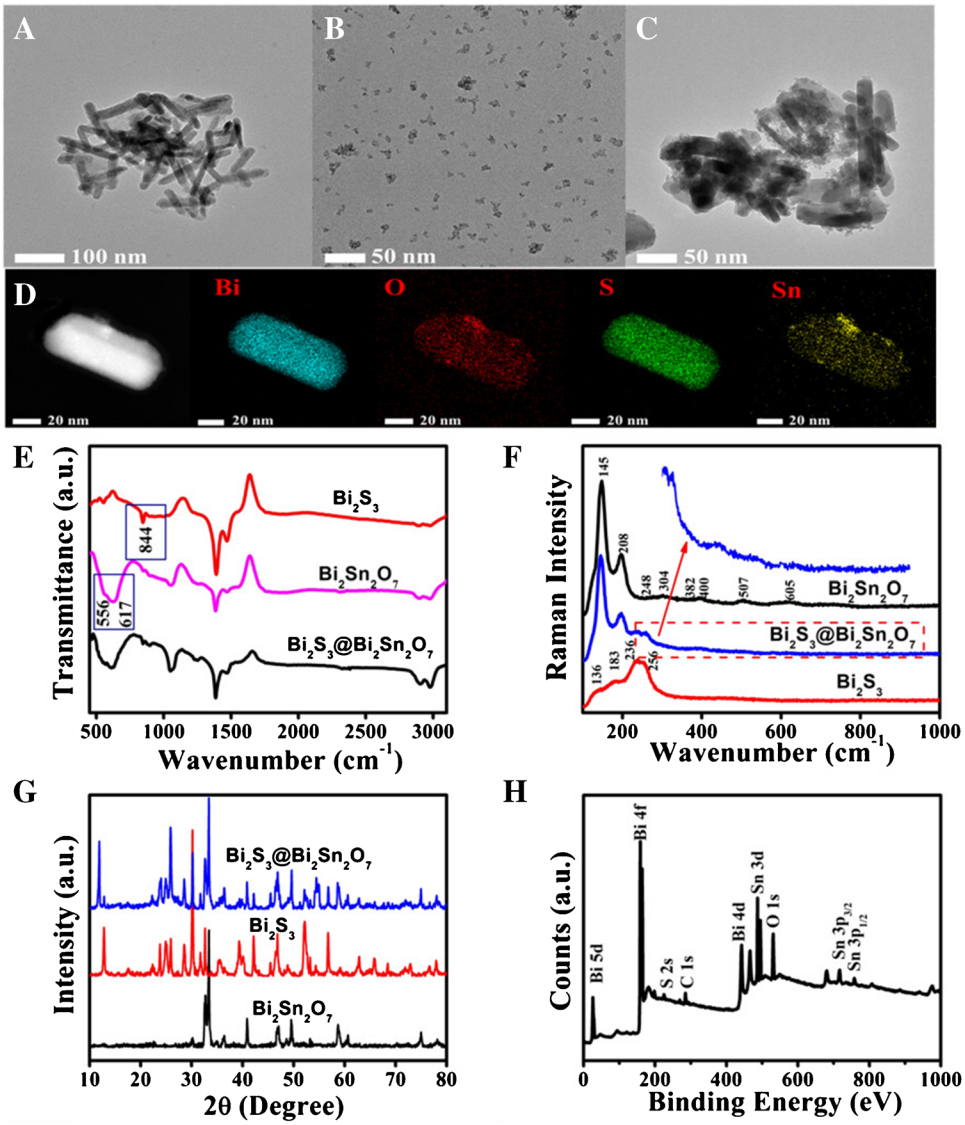

Fig. 1 TEM images of (**A**) Bi_2S_3, (**B**) $Bi_2Sn_2O_7$, and (**C**) Bi_2S_3@$Bi_2Sn_2O_7$; (**D**) element mapping map of Bi_2S_3@$Bi_2Sn_2O_7$ (Bi, O, S, Sn); (**E**) FT-IR, (**F**) Raman, and (**G**) XRD spectra of $Bi_2Sn_2O_7$, Bi_2S_3, and Bi_2S_3@$Bi_2Sn_2O_7$ heterojunction; (**H**) XPS spectrum of Bi_2S_3@$Bi_2Sn_2O_7$ heterojunction

162.6 eV) and Bi $4f_{5/2}$ (158.4 eV, 163.8 eV), indicating the existence of Bi^{3+}. The characteristic peak of S 2p between Bi $4f_{7/2}$ and Bi $4f_{5/2}$ is S $2p_{3/2}$ (160.6 eV), indicating the existence of S^{2-}. The peaks of Sn $3d_{5/2}$ (486.3e V) and Sn $3d_{3/2}$ (494.6e V) at the same time indicate that Sn^{4+} exists in the heterojunction, and the binding energy of O 1 s is at 530.1 eV, indicating that the sample contains oxygen, which is consistent with other literatures [32].

Light absorption capacity is an important indicator to measure photoelectric materials. As can be seen from the UV–Vis diffuse reflectance spectrum (UV–Vis DRS) of the sample in Fig. S3A, the light absorption range of pure Bi_2S_3 is relatively strong, with a certain absorption capacity almost in the whole visible region. In contrast, the light absorption efficiency of $Bi_2Sn_2O_7$ is relatively low, and it mainly absorbs light below 437 nm, so the range is limited to the visible region. By simple physical adsorption method, $Bi_2Sn_2O_7$ was attached to the surface of Bi_2S_3. It can be found that due to the synergistic effect between Bi_2S_3 and $Bi_2Sn_2O_7$, the absorption wavelength shifts to the visible region, which greatly improves the utilization efficiency of visible light of Bi_2S_3@$Bi_2Sn_2O_7$ heteroconjugation [33].

In addition, the band gap of the material was calculated according to the Tauc formula:

$\alpha h\nu = A(h\nu\text{-}Eg)^{n/2}$; α is the absorption coefficient, h is Planck's constant, Eg is the band gap, and A is a constant. The value of n is related to the type of electronic transition. For direct transition semiconductors such as Bi_2S_3, $n=1$; for indirect transition semiconductors such as $Bi_2Sn_2O_7$, $n=4$. Eg is obtained by Taul linear region extrapolation. And it can be seen from Fig. S3B that the Eg values of Bi_2S_3 and $Bi_2Sn_2O_7$ are 1.39 eV and 2.65 eV, respectively, which are similar to the values reported in the literature [34]. The conduction band potential (E_{CB}) and valence band potential

(E_{VB}) of Bi_2S_3 and $Bi_2Sn_2O_7$ were calculated according to the following formula [35]: $E_{VB} = X - E_0 + 0.5Eg$, $E_{CB} = E_{VB} - Eg$, where X is the absolute electronegativity of the semiconductor and E_0 is the free electron potential energy (4.5 eV) in a standard hydrogen electrode. The X values of Bi_2S_3 and $Bi_2Sn_2O_7$ are 5.28 eV and 6.08 eV, respectively. The E_{CB} of Bi_2S_3 and $Bi_2Sn_2O_7$ are calculated to be 0.09 eV and 0.26 eV, respectively, and the E_{VB} are 1.48 eV and 2.91 eV, respectively. Figure S3C is the schematic diagram of the energy levels of Bi_2S_3 and $Bi_2Sn_2O_7$, indicating that Bi_2S_3 and $Bi_2Sn_2O_7$ can form heterojunction, resulting in the enhancement of PEC activity and stability.

Electrochemical characterizations of the sensing system

To ensure the successful synthesis of Bi_2S_3@$Bi_2Sn_2O_7$ heterojunctions, the photocurrents of different materials modified on the surface of GCE were firstly measured by PEC characterization. As shown in Fig. 2A, the photocurrent signal of GCE/Bi_2S_3@$Bi_2Sn_2O_7$ (curve c) is significantly higher than that of GCE/$Bi_2Sn_2O_7$ (curve a) and GCE/Bi_2S_3 (curve b), indicating that Bi_2S_3@$Bi_2Sn_2O_7$ heterojunction itself can greatly improve the photocurrent activity. Figure S4 illustrates the possible electron transfer mechanism during photocurrent generation. Under the irradiation of visible light, Bi_2S_3@$Bi_2Sn_2O_7$ is excited by light to generate photogenerated electron–hole pairs. Because the positions of the conduction band (CB) and valence band (VB) of Bi_2S_3 are more negative than those of $Bi_2Sn_2O_7$. This allows the photogenerated electrons to be transferred from the CB of Bi_2S_3 to the CB of $Bi_2Sn_2O_7$, and the photogenerated holes to be transferred from the VB of $Bi_2Sn_2O_7$ to the VB of Bi_2S_3, thereby initially realizing the separation of space charges, and the introduction of the electron donor AA can effectively suppress the electron holes recombination which improves the photoelectric conversion efficiency, thereby enhancing the photocurrent signal. In order to further characterize the photoelectric activity of the material, a series of electrochemical tests were carried out; EIS and CV were selected to characterize the different materials modified on the electrode surface. As displayed in Fig. 2B and Fig. S5, compared with the bare GCE electrode (curve a), the GCE/$Bi_2Sn_2O_7$ (curve b), GCE/Bi_2S_3 (curve c), and GCE/Bi_2S_3@$Bi_2Sn_2O_7$ (curve d) all exhibit the reduced electrochemical current signal and the increased EIS value, because the conductivity of the semiconductor material itself is relatively weak, which will greatly hinder the transfer of electrons from the redox probes in the electrolyte to the electrode surface. Compared with GCE/$Bi_2Sn_2O_7$ (curve b), GCE/Bi_2S_3 (curve c) modified electrodes, GCE/Bi_2S_3@$Bi_2Sn_2O_7$ (curve d) exhibited strong CV current signals and reduced EIS values, indicating the formation of Bi_2S_3@$Bi_2Sn_2O_7$ heterojunctions can improve the conductivity of the material and increase the rate of electron transfer on the electrode surface [36]. All these results further indicate the successful synthesis of Bi_2S_3@$Bi_2Sn_2O_7$ heterojunction.

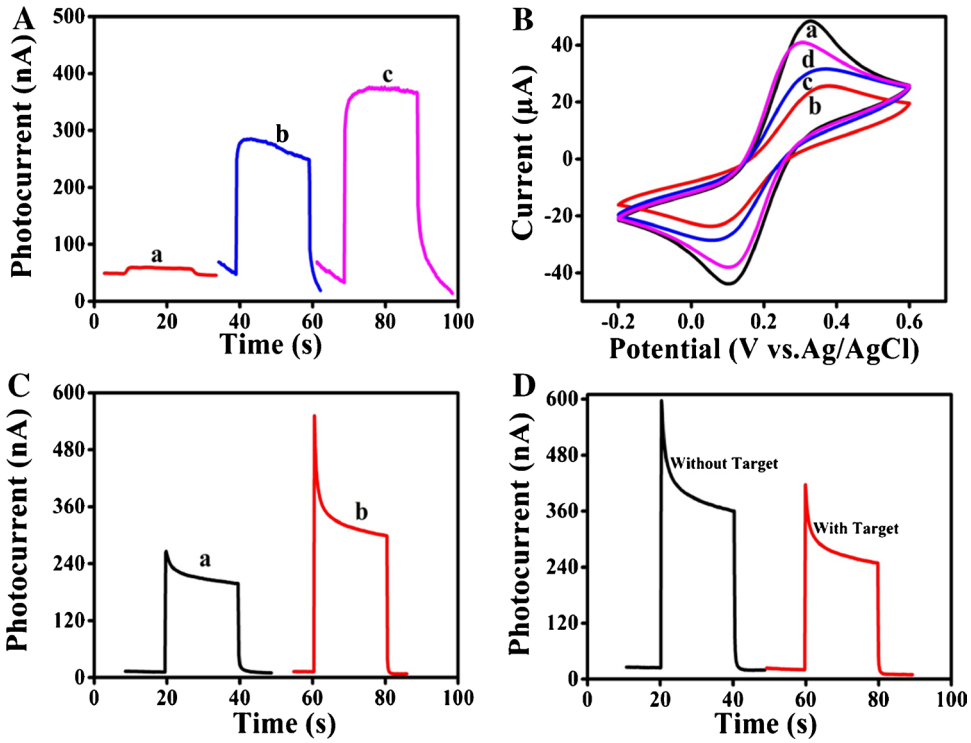

Fig. 2 **A** Photocurrent response of (curve a) $Bi_2Sn_2O_7$, (curve b) Bi_2S_3, and (curve c) Bi_2S_3@$Bi_2Sn_2O_7$ in PBS (10 mmol L^{-1}, pH 7.4) containing 50 mmol L^{-1} AA. **B** CV profiles of (curve a) GCE, (curve b) GCE/$Bi_2Sn_2O_7$, (curve c) GCE/Bi_2S_3, and (curve d) GCE/Bi_2S_3@$Bi_2Sn_2O_7$ in 2.5 mmol L^{-1} $[Fe(CN)_6]^{3-/4-}$ PBS solution containing 0.05 mol L^{-1} KCl. **C** Photocurrent response of Bi_2S_3@$Bi_2Sn_2O_7$ in (curve a) PBS solution and (curve b) ALP enzyme-catalyzed production of AA in PBS solution, $C_{[OM]} = 1$ ng mL^{-1}. **D** Photocurrent response of biosensor constructed by Bi_2S_3@$Bi_2Sn_2O_7$ without or with the reaction of target, $C_{[OM]} = 10$ ng $mL.^{-1}$

Feasibility analysis of PEC biosensor

To further demonstrate that the produced AA can serve as an electron donor and play a role in increasing photocurrent signal, the photocurrent signal of AA catalyzed by ALP enzyme-based biosensor constructed based on Bi_2S_3@$Bi_2Sn_2O_7$ is studied in Fig. 2C. It is found that in the absence of electron donor AA, a weak photocurrent signal (curve a) is generated due to electron–hole recombination due to light generation. In the presence of AA (curve b), the photocurrent signal is significantly enhanced because AA acts as an electron donor and is oxidized by the holes generated by light, thus inhibiting the electron–hole recombination. Figure 2D shows the activity of the ALP enzyme is reduced by OPs-based enzyme inhibition in the presence of 10 ng mL^{-1}; thus, the AA generated by enzymic catalytic hydrolysis also decreases, resulting in a significant decrease in the photocurrent signal compared with the absence of OM. According to this relationship, sensitive detection of OM with different concentrations can be achieved.

Optimization of the detection conditions

To achieve the best analytical performance of the constructed PEC biosensing system, the materials and experimental conditions were optimized. Among them, the concentration and mass ratio of Bi_2S_3@$Bi_2Sn_2O_7$ mixed materials have a significant impact on the photocurrent signal. Since the mass ratio of the heterojunction material ($Bi_2Sn_2O_7$:Bi_2S_3) directly affects the effective separation of electron–hole pairs and thus has a greater impact on the photocurrent, it is firstly investigated. As shown in Fig. S6A, the photocurrent signal is the largest with the value of 416 nA when the mass ratio is 1:3, which is because the Bi_2S_3 inhibits the recombination of photoinduced electron–hole pairs in $Bi_2Sn_2O_7$. When the Bi_2S_3 content is appropriate, the photoinduced electron–hole pairs recombination can be well inhibited and a large photocurrent signal can be generated. Therefore, the photocurrent signals generated by Bi_2S_3@$Bi_2Sn_2O_7$ heterojunctions were measured at a material ratio of 1:3. Meanwhile, Bi_2S_3@$Bi_2Sn_2O_7$ serves as a substrate for photoactive materials, and its concentration is also an important parameter for constructing PEC biosensors. As shown in Fig. S6B, the photocurrent signals first increase with the increase of the heterojunction concentration. The photocurrent signal is the largest with the value of 430 nA when the heterojunction concentration is 3 mg mL^{-1} and then reduces to 280 nA at 5 mg mL^{-1}. This is because the excessive Bi_2S_3@$Bi_2Sn_2O_7$ mixture will form a steric hindrance effect on the electrode surface due to the increase of the film thickness, which will significantly increase the diffusion resistance of the hole movement in the film and thus causing the photocurrent signal to gradually decrease [37]. Therefore, the heterojunction material with a concentration of 3 mg mL^{-1} and a mass ratio ($Bi_2Sn_2O_7$:Bi_2S_3 = 1:3) was selected to construct the sensing electrode in the subsequent experiments.

Next, the experimental conditions were optimized under the optimal mass ratio and concentration of Bi_2S_3@$Bi_2Sn_2O_7$ heterojunction materials obtained above. When the concentration of OM was 10 ng mL^{-1}, the effects of OM inhibition time on ALP enzyme activity, AAP concentration, ALP hydrolysis time of AAP, and ALP concentration on photocurrent signal in the constructed PEC biosensor were investigated. This PEC sensor is mainly based on the enzymatic inhibition of OM on ALP to indirectly achieve a quantitative analysis of OM, so the time of OM inhibiting ALP activity is crucial in the whole experiment. As can be seen in Fig. S7A, when the inhibition time is extended from 10 to 30 min, the photocurrent signal declines significantly, which is because the inhibition effect of OM on ALP reduces the enzyme activity, and the electron donor AA generated by catalytic hydrolysis also decreases, leading to the photoinduced electron–hole reorganization in Bi_2S_3@$Bi_2Sn_2O_7$ heterojunction. When the inhibition time exceeded 30 min, the photocurrent change could be ignored, indicating that the catalytic activity of the OM inhibitor had reached saturation within 30 min, so 30 min was selected as the best inhibition time. As the catalytic substrate of ALP, the concentration of AAP will also directly affect the amount of electron donor AA generated by enzymatic hydrolysis, and further affect the strength of the photocurrent signal in the PEC sensor. As shown in Fig. S7B, the photocurrent signal is significantly enhanced with the increase of AAP concentration from 15 to 25 mmol L^{-1}, which is due to the AA as an electron donor is increased and enhancing the separation of photogenerated electron holes in Bi_2S_3@$Bi_2Sn_2O_7$ heterojunctions. When the AAP concentration exceeds 25 mmol L^{-1}, the photocurrent signal is almost stable, because the reaction between ALP and AAP has reached the equilibration, so 25 mmol L^{-1} is selected as the optimal concentration of AAP. In addition, the time of ALP hydrolysis of AAP also affects the generation of AA, thus further affecting the strength of the photocurrent signal. As depicted in Fig. S7C, the photocurrent signal increases gradually with the increase of the catalytic hydrolysis time from 10 to 30 min, because the prolonged reaction time will generate more AA to provide more electrons to neutralize the holes, thus effectively inhibiting the reorganization of the photogenerated electron–hole pair. Furthermore, it reaches the plateau and hydrolysis is complete after 30 min, indicating that 30 min is the best time for enzymatic hydrolysis. In Fig. S7D, the influence of ALP concentration on photocurrent was investigated. The photocurrent signal shows an upward trend from 10 to 50 U L^{-1}, because the higher the concentration of ALP, the more AA is produced by the hydrolysate of the enzyme. When

it reaches 50 U L^{-1}, the reaction between ALP and AAP has reached saturation and the reaction rate has reached the maximum, so the photocurrent signal reaches the plateau state. Then, 50 U L^{-1} of ALP was selected for the subsequent experimental process.

Analytical performance of the PEC sensor

To ensure the practicality of the PEC biosensor constructed by Bi_2S_3@$Bi_2Sn_2O_7$ for OM detection, quantitative detection of OM with different concentrations was carried out under optimal conditions. As given in Fig. 3A and 3B, the photocurrent signal gradually decreases with the increase of OM concentration. This is based on the enzyme inhibition effect of OM, which reduces the activity of the ALP enzyme and reduces the electron donor AA generated by catalytic hydrolysis, thus reducing the photocurrent signal of the constructed PEC biosensor. As can be seen from the inset of Fig. 3B, there is a linear relationship between the change of photocurrent and the log value of OM concentration, ranging from 0.05 to 500 ng mL^{-1}. The linear regression equation is $I = -53.63 \times \mathrm{LgC}_{[\mathrm{OM}]} + 287.46$, and the correlation coefficient (R^2) is 0.9984. The limit of detection (LOD) is 0.01465 ng mL^{-1} (3SD/K, SD is the standard deviation of PEC current signal measured by 11 blank samples; K is the slope of the linear equation). As shown in Table S1, the detection performance of our self-constructed PEC biosensor was also compared with the previously reported methods for OM detection. The sensitivity of our PEC biosensor was comparable or even higher than other OM determination methods [38–44]. The homogeneous PEC method showed relatively high sensitivity because of the combination of optical advantages with electrical advantages and homogeneous system. However, compared with the electrochemical sensor [45] and ECL aptasensor [46], the sensitivity of the homogeneous PEC method was relatively low within a narrow linear range. This was because the 3D M-Co_3O_4-modified sensing platform together with the conductive graphdiyne achieved significant electrochemical signal amplification, resulting in favorable sensitivity. By integration of as-prepared ZIF-8-$MoTe_2$ with specificity OM aptamer, the ECL sensor showed a broad linear range within a comparatively low detection limit. Therefore, the self-constructed homogeneous PEC detection showed an acceptable detection sensitivity and linear range for OM.

Subsequently, we evaluated the reproducibility and stability of the PEC sensor platform. The intra-batch and inter-batch repeatability was evaluated by measuring OM at three different concentrations (0.05 ng mL^{-1}, 50 ng mL^{-1}, and 500 ng mL^{-1}) as can be seen in Fig. S8. The coefficient of variation (CV) for the intra-batch determination results was 1.02%, 1.33%, and 1.75% ($n = 3$), respectively. The coefficients of variation between batches were 2.69%, 2.24%, and 2.42% ($n = 3$), respectively. In addition, the stability of the PEC sensor platform was also studied. As shown in Fig. 3C, the photocurrent signal intensity hardly changes significantly after 7 consecutive lamp on/off cycles within 300 s; the photocurrent remains 89.46% ($C_{\mathrm{OM}} = 0$ ng mL^{-1}, black color) and 89.17% ($C_{\mathrm{OM}} = 10$ ng mL^{-1}, red color) of the initial current, indicating that the sensor has good stability. The

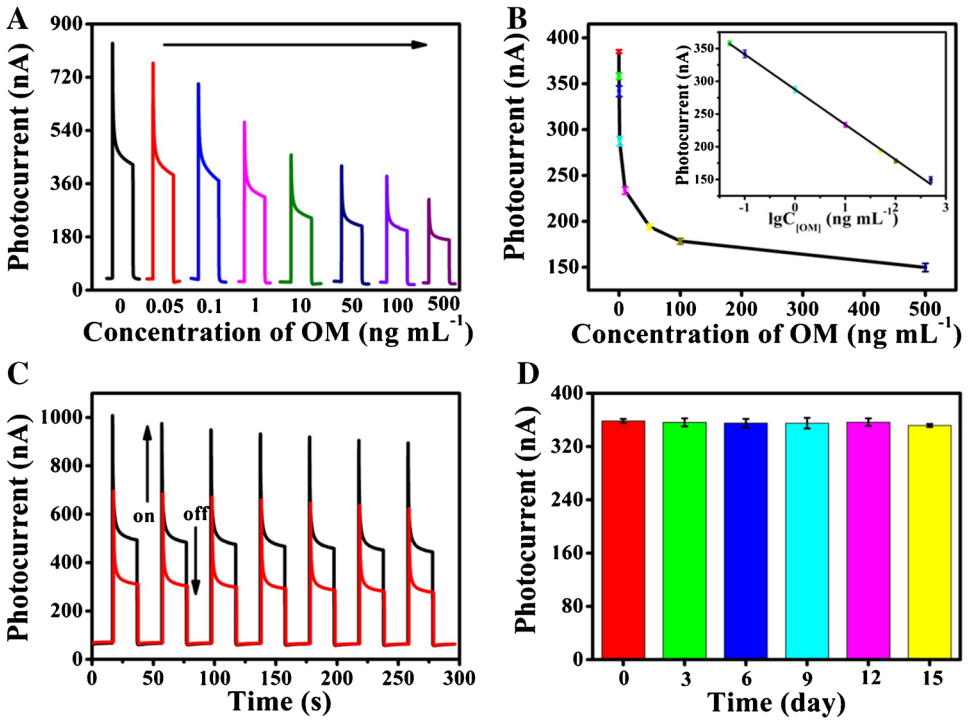

Fig. 3 **A** PEC response intensity of the sensor to OM at different concentrations. **B** The relationship between OM concentration and PEC response intensity (inset shows the linear relationship between PEC response intensity and $\mathrm{lgC}_{[\mathrm{OM}]}$). **C** Stability test of self-constructed PEC sensing platform. **D** Investigation of the storage stability in the presence of OM (0.05 ng $mL.^{-1}$) for every 3 days (error bars: SD, $n = 3$)

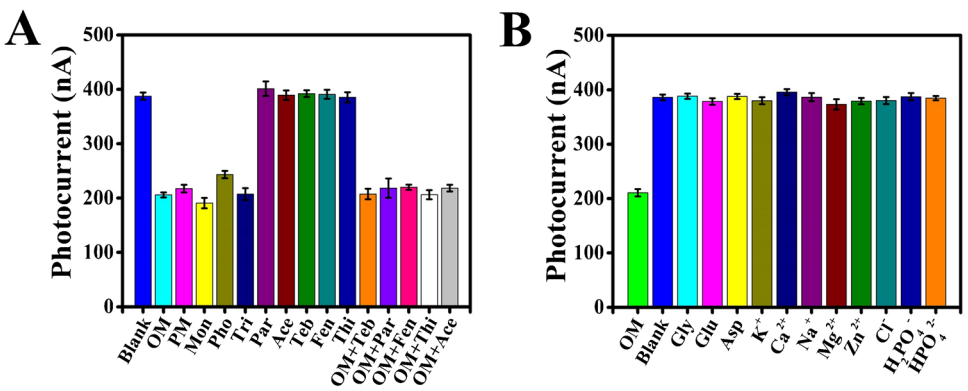

Fig. 4 **A** Selectivity of the self-constructed PEC sensing platform: the concentration of OM was 50 ng mL^{-1}, and the concentration of other pesticides was 5000 ng mL^{-1} (100 times); **B** effect of coexisting substance on the PEC response intensity: the concentration of OM was 50 ng mL^{-1}, and the concentration of coexisting substance was 5000 ng $mL.^{-1}$ (100 times) (error bars: SD, $n = 3$)

constructed PEC sensor platform ($C_{OM} = 0.05$ ng mL^{-1}) is placed in 4 ℃ darkness for 15 days, as shown in Fig. 3D, the photocurrent signal remains 98.07% of the initial current signal with the value of 351.6 nA, and the maximum relative standard deviation (RSD) does not exceed 8%. The experimental data showed that the proposed PEC biosensor had good stability and long-term storage properties. In brief, the sensor had satisfactory stability and reproducibility.

The selectivity and anti-interference of PEC biosensor for OM detection

In terms of the performance of self-constructed sensors, selectivity and anti-interference capability are also more important factors, which determine the application range of the sensor. To assess the selectivity of the PEC sensor based on Bi_2S_3@$Bi_2Sn_2O_7$ for OM, several other common OPs such as methyl parathion (PM), monocrotophos (Mon), phorate (Pho), and triazophos (Tri)) were investigated. Additionally, the sensing platform was also used to detect several common non-OPs such as paraquat (Par), fenvalerate (Fen), thiamethoxam (Thi), acetochlor (Ace), and tebuconazole (Teb). As shown in Fig. 4A, the use of non-OPs does not cause significant photocurrent changes compared with the blank group which is about 395 nA. When omethoate (OM) is mixed with non-OPs, the detection results are basically consistent with the photocurrent signal generated by pure OM. The use of several other common OPs all causes the reduction of the photocurrent signal and the photocurrent signal is reduced to half of the blank group which is about 200 nA, which is caused by the inhibitory effect of OPs on the ALP enzyme activity. All these results showed that the constructed PEC sensing platform had good selectivity and could be used for the detection of other OPs.

In addition, it is considered that some coexisting ionic electrolytes and bioactive molecules will affect the detection effect of the experiment during the actual sample detection process. Therefore, three kinds of amino acids such as glutamic acid (Glu), glycine (Gly), and L-aspartic acid (Asp), five kinds of cationic electrolytes (K^+, Ca^{2+}, Na^+, Mg^{2+}, Zn^{2+}), and three kinds of anion electrolytes (Cl^-, $H_2PO_4^-$, HPO_4^{2-}) were selected. As shown in Fig. 4B, the response photocurrent obtained by the addition of these interfering substances is almost close to the current signal value of the blank group for about 400 nA, without causing significant changes in the photocurrent signal. These experimental data showed that the sensor had good anti-interference for the detection of OM.

OM detection in real samples

To further evaluate the application potential of the self-constructed PEC biosensing platform, this PEC analysis method was selected to detect OM in vegetable samples. By the standard addition method, different concentrations of OM standard solutions were added to the pretreated vegetable samples to measure the photocurrent and calculated the recovery rate. The results are shown in Table S2; the recoveries ranged from 83.8 to 114.1%. In addition, the maximum RSD did not exceed 10%. To further verify the accuracy of the method in the detection of actual samples, the results of the PEC detection method and the HPLC reference results were compared with each other. As can be shown in Table 1, the detection results of the two methods are almost similar. It shows that the PEC detection method is feasible and can be used for the detection of OM in vegetable samples.

Conclusions

In summary, we developed a novel homogeneous photoelectrochemical sensing platform based on ALP-mediated pesticide assay and Bi_2S_3@$Bi_2Sn_2O_7$ heterojunction for

Table 1 Comparison of the results between HPLC and PEC methods in the determination of OM in vegetables ($n=3$)

Sample	Added (μg mL^{-1})	HPLC method Found ± SD (RSD) (μg mL^{-1})	Dilution ratio (final concentration) (ng mL^{-1})	PEC method Found ± SD (RSD) (ng mL^{-1}) (ng mL^{-1})
Spinach	0.5	0.44 ± 0.001 (0.2%)	10^4 (0.044)	0.042 ± 0.003 (7.1%)
	5	4.91 ± 0.015 (0.3%)	10^2 (49.15)	48.60 ± 1.42 (2.9%)
	10	10.05 ± 0.042 (0.4%)	30 (334.93)	335.15 ± 11.78 (3.5%)
Mustard	0.5	0.46 ± 0.002 (0.4%)	10^4 (0.046)	0.044 ± 0.002 (4.5%)
	5	4.98 ± 0.054 (1.1%)	10^2 (49.76)	49.93 ± 1.65 (3.3%)
	10	10.03 ± 0.030 (0.3%)	30 (334.45)	335.36 ± 7.51 (2.2%)

the sensitive detection of OM. Both the activity inhibition of ALP enzyme and PEC determination were performed in the homogeneous phase, which avoided the labeling and multiple tedious washing steps and immobilization procedures, improving the stability and reproducibility of the PEC sensor. Furthermore, the construction difficulty and time cost of PEC for OPs determination were greatly reduced. The Bi_2S_3@$Bi_2Sn_2O_7$ heterojunction was used as the substrate material of the biosensor, which had excellent photoelectrochemical properties and generated a sustained and stable background photocurrent signal. The construction of the sensor was mainly based on the inhibitory effect of OPs on the enzymatic activity of ALP, so that the electron donor AA produced by catalytic hydrolysis would also decrease, thereby reducing the measured photocurrent signal to achieve a quantitative analysis of the OM. Compared with other analysis methods for OM detection, this homogeneous PEC biosensor combined ALP-mediated pesticide assay, which exhibited a wide linear range and a low detection limit with good reproducibility, stability, and selectivity. Even in actual sample detection, satisfactory recovery values were obtained from this PEC biosensor. Hence, the self-constructed PEC biosensor provides a new idea for the detection of OPs residues, and has great application potential in the field of food safety and healthcare detection. Future work will focus on the integration of homogeneous PEC sensing techniques with a portable device for improving practicality.

Supplementary Information The online version contains supplementary material available at https://doi.org/10.1007/s00216-022-04279-x.

Funding The authors received financial support from the National Natural Science Foundation (21964004, 22164005) and the Natural Science Foundation of Guangxi (2022GXNSFAA035475).

Declarations

Conflict of interest The authors declare no competing interests.

References

1. Khatun MA, Hoque MA, Zhang Y, Lu T, Cui L, Zhou NY, et al. Bacterial consortium-based sensing system for detecting organophosphorus pesticides. Anal Chem. 2018;90(17):10577–84. https://doi.org/10.1021/acs.analchem.8b02709.
2. Pundir CS, Malik A, Preety. Bio-sensing of organophosphorus pesticides: a review. Biosens Bioelectron. 2019;140:111348. https://doi.org/10.1016/j.bios.2019.111348.
3. Li Q, Wu JH, Yang QT, Li HY, Li F. pH and redox dual-response disulfide bond-functionalized red-emitting gold nanoclusters for monitoring the contamination of organophosphorus pesticides in foods. Anal Chem. 2021;93(19):7362–8. https://doi.org/10.1021/acs.analchem.1c01414.
4. Yu SY, Zhang L, Zhu LB, Gao Y, Fan GC, Han DM, et al. Bismuth-containing semiconductors for photoelectrochemical sensing and biosensing. Coord Chem Rev. 2019;393:9–20. https://doi.org/10.1016/j.ccr.2019.05.008.
5. Wang J, Liu ZH. Recent advances in two-dimensional layered materials for photoelectrochemical sensing. TrAC, Trends Anal Chem. 2020;133: 116089. https://doi.org/10.1016/j.trac.2020.116089.
6. Zang Y, Fan J, Ju Y, Xue HG, Pang H. Current advances in semiconductor nanomaterial-based photoelectrochemical biosensing chemistry. A European Journal. 2018;24(53):14010–27. https://doi.org/10.1002/chem.201801358.
7. Li HY, Qi HJ, Chang JF, Gai PP, Li F. Recent progress in homogeneous electrochemical sensors and their designs and applications. TrAC, Trends Anal Chem. 2022;156: 116712. https://doi.org/10.1016/j.trac.2022.116712.
8. Wang XY, Rong XJ, Zhang Y, Luo F, Qiu B, Wang J, et al. Homogeneous photoelectrochemical aptasensors for tetracycline based on sulfur-doped g-C_3N_4/n-GaN heterostructures formed through self-assembly. Anal Chem. 2022;94(8):3735–42. https://doi.org/10.1021/acs.analchem.2c00118.
9. Song X, Hou T, Lu FF, Wang YZ, Liu JJ, Li F. Homogeneous photoelectrochemical biosensing via synergy of G-quadruplex/hemin catalysed reactions and the inner filter effect. Chem Commun. 2020;56(12):1811–4. https://doi.org/10.1039/C9CC09280C.
10. Wang H, Yuan F, Wu XM, Dong YM, Wang GL. Enzymatic in situ generation of covalently conjugated electron acceptor of PbSe quantum dots for high throughput and versatile photoelectrochemical bioanalysis. Anal Chim Acta. 2019;1058:1–8. https://doi.org/10.1016/j.aca.2019.01.057.
11. Liu XJ, Song MM, Hou T, Li F. Label-free homogeneous electroanalytical platform for pesticide detection based on acetylcholinesterase-mediated DNA conformational switch integrated with

rolling circle amplification. ACS Sens. 2017;2(4):562–8. https://doi.org/10.1021/acssensors.7b00081.
12. Zheng DL, Chen M, Chen YW, Gao WH. In-situ preparation of hollow $CdCoS_2$ heterojunction with enhanced photocurrent response for highly photoelectrochemical sensing of organophosphorus pesticides. Anal Chim Acta. 2022;1212: 339913. https://doi.org/10.1016/j.aca.2022.339913.
13. Qin Y, Wu Y, Chen GJ, Jiao L, Hu LY, Gu WL, et al. Dissociable photoelectrode materials boost ultrasensitive photoelectrochemical detection of organophosphorus pesticides. Anal Chim Acta. 2020;1130:100–6. https://doi.org/10.1016/j.aca.2020.07.036.
14. Hou L, Qin YX, Li JY, Qin SY, Huang YL, Lin TR, et al. A ratiometric multicolor fluorescence biosensor for visual detection of alkaline phosphatase activity via a smartphone. Biosens Bioelectron. 2019;143: 111605. https://doi.org/10.1016/j.bios.2019.111605.
15. Yuan L, Gan Z, Fan Y, Ding F, Xu X, Chen X, et al. Thermal-controlled active sensor module using enzyme-regulated UiO-66-NH_2/MnO_2 fluorescence probe for total organophosphorus pesticide determination. J Hazard Mater. 2022;436: 129111. https://doi.org/10.1016/j.jhazmat.2022.129111.
16. Cai Y, Qiu ZY, Lin XB, Zeng W, Cao YR, Liu WP, et al. Self-assembled nanomaterials based on aggregation-induced emission of AuNCs: fluorescence and colorimetric dual-mode biosensing of organophosphorus pesticides. Sens Actuators, B. 2020;321. https://doi.org/10.1016/j.snb.2020.128481
17. Chu YH, Li Y, Wang YT, Li B, Zhang YH. Investigation of interaction modes involved in alkaline phosphatase and organophosphorus pesticides via molecular simulations. Food Chem. 2018;254:80–6. https://doi.org/10.1016/j.foodchem.2018.01.187.
18. Wang Q, Ruan YF, Zhao WW, Lin P, Xu JJ, Chen HY. Semiconducting organic–inorganic nanodots heterojunctions: platforms for general photoelectrochemical bioanalysis application. Anal Chem. 2018;90(6):3759–65. https://doi.org/10.1021/acs.analchem.7b03852.
19. Xu WC, Fang JZ, Chen YF, Lu SY, Zhou GY, Zhu XM, et al. Novel heterostructured Bi_2S_3/$Bi_2Sn_2O_7$ with highly visible light photocatalytic activity for the removal of rhodamine B. Mater Chem Phys. 2015;154:30–7. https://doi.org/10.1016/j.matchemphys.2015.01.040.
20. Wang M, Yin HS, Shen NN, Xu ZN, Sun B, Ai SY. Signal-on photoelectrochemical biosensor for microRNA detection based on Bi_2S_3 nanorods and enzymatic amplification. Biosens Bioelectron. 2014;53:232–7. https://doi.org/10.1016/j.bios.2013.09.069.
21. Leng DQ, Li JS, Xu R, Liu L, Liu XJ, Fan DW, et al. THCH as electron donor in controlled-release system for procalcitonin analysis based on $Bi_2Sn_2O_7$ photoanode. Sens Actuators, B. 2020;321: 128509. https://doi.org/10.1016/j.snb.2020.128509.
22. Xi JJ, Wang H, Zhang BH, Zhao FQ, Zeng BZ. Novel molecularly imprinted photoelectrochemical sensor for rutin based on Bi_2S_3/$ZnIn_2S_4$ heterojunction. Sens Actuators, B. 2020;320: 128409. https://doi.org/10.1016/j.snb.2020.128409.
23. Guo H, Niu CG, Zhang L, Wen XJ, Liang C, Zhang XG, et al. Construction of direct Z-scheme AgI/$Bi_2Sn_2O_7$ nanojunction system with enhanced photocatalytic activity: accelerated interfacial charge transfer induced efficient Cr(VI) reduction, tetracycline degradation and escherichia coli inactivation. ACS Sustainable Chem Eng. 2018;6(6):8003–18. https://doi.org/10.1021/acssuschemeng.8b01448.
24. Shi XX, Li XQ, Wei XP, Li JP. Molecularly imprinted photoelectrochemical sensor based on $AgBiS_2$/$Bi2S_3$ for determination of propoxur. Chin J Anal Chem. 2020;48(3):396–404. https://doi.org/10.1016/S1872-2040(20)60004-4.
25. Hu CC, Zhuang J, Zhong LS, Zhong Y, Wang DH, Zhou HY. Significantly enhanced photocatalytic activity of visible light responsive AgBr/$Bi_2Sn_2O_7$ heterostructured composites. Appl Surf Sci. 2017;426:1173–81. https://doi.org/10.1016/j.apsusc.2017.07.167.
26. Li N, Sun YN, Wang FY, Huang C, Fu CP, Zhang LN, et al. Target dual-recycling-induced bipedal DNA walker and Bi_2WO_6/Bi_2S_3 cascade amplification strategy in photoelectrochemical biosensor for TP53 detection. Sens Actuators, B. 2021;345: 130386. https://doi.org/10.1016/j.snb.2021.130386.
27. Cao JT, Lv JL, Liao XJ, Ma SH, Liu YM. Photogenerated hole-induced chemical–chemical redox cycling strategy on a direct Z-scheme Bi_2S_3/Bi_2MoO_6 heterostructure photoelectrode: toward an ultrasensitive photoelectrochemical immunoassay. Anal Chem. 2021;93(28):9920–6. https://doi.org/10.1021/acs.analchem.1c02175.
28. Silva RX, Paschoal CWA, Almeida RM, Castro MC, Ayala AP, Auletta JT, et al. Temperature-dependent raman spectra of $Bi_2Sn_2O_7$ ceramics. Vib Spectrosc. 2013;64:172–7. https://doi.org/10.1016/j.vibspec.2012.05.009.
29. Caglar B, Guner EK, Ersoy S, Caglar S, Özdemir AO, Özdokur KV, et al. Bi_2S_3 nanorods decorated on bentonite nanocomposite for enhanced visible-light-driven photocatalytic performance towards degradation of organic dyes. J Alloys Compd. 2021;885: 160964. https://doi.org/10.1016/j.jallcom.2021.160964.
30. Lu Y, Huang Y, Jj Cao, Ho WK, Zhang Q, Zhu DD, et al. Insight into the photocatalytic removal of NO in air over nanocrystalline $Bi_2Sn_2O_7$ under simulated solar light. Ind Eng Chem Res. 2016;55(40):10609–17. https://doi.org/10.1021/acs.iecr.6b02514.
31. Wang FX, Ye C, Mo S, Liao LL, Luo HQ, Li NB. A novel photoelectrochemical sensing platform based on Fe_2O_3@Bi_2S_3 heterojunction for an enzymatic process and enzyme activity inhibition reaction. Sens Actuators, B. 2019;288:202–9. https://doi.org/10.1016/j.snb.2019.02.121.
32. Cao JT, Wang B, Dong YX, Wang Q, Ren SW, Liu YM, et al. Photogenerated hole-induced chemical redox cycling on Bi_2S_3/$Bi_2Sn_2O_7$ heterojunction: toward general amplified split-type photoelectrochemical immunoassay. ACS Sens. 2018;3(6):1087–92. https://doi.org/10.1021/acssensors.8b00332.
33. Li J, Xiong P, Tang J, Liu L, Gao S, Zeng Z, et al. Biocatalysis-induced formation of BiOBr/Bi_2S_3 semiconductor heterostructures: a highly efficient strategy for establishing sensitive photoelectrochemical sensing system for organophosphorus pesticide detection. Sens Actuators, B. 2021;331: 129451. https://doi.org/10.1016/j.snb.2021.129451.
34. Li HK, Cai QQ, Yan XS, Jie G. Target-switchable DNA hydrogels coupled with a $Bi_2Sn_2O_7$/Bi_2S_3 heterojunction based on in situ anion exchange for the "signal-on" photoelectrochemical detection of DNA. Nanoscale. 2021;13(16):7678–84. https://doi.org/10.1039/D1NR00573A.
35. Wang H, Ye H, Zhang B, Zhao F, Zeng B. Synthesis of $ZnIn_2S_4$/CdS heterostructure based on electrostatic interaction mechanism for indirect photoelectrochemical detection of dopamine. J Phys Chem C. 2018;122(35):20329–36. https://doi.org/10.1021/acs.jpcc.8b05287.
36. Liao XJ, Xiao HJ, Cao JT, Ren SW, Liu YM. A novel split-type photoelectrochemical immunosensor based on chemical redox cycling amplification for sensitive detection of cardiac troponin I. Talanta. 2021;233: 122564. https://doi.org/10.1016/j.talanta.2021.122564.
37. Cheng WJ, Zheng ZY, Yang JY, Chen M, Yao QW, Chen YW, et al. The visible light-driven and self-powered photoelectrochemical biosensor for organophosphate pesticides detection based on nitrogen doped carbon quantum dots for the signal amplification. Electrochim Acta. 2019;296:627–36. https://doi.org/10.1016/j.electacta.2018.11.086.
38. Zhang H, Kang WK, Wang Y, Wang XZ, Lu LH. An enzymatic reaction modulated fluorescence-on omethoate biosensor based on Fe_3O_4@GO and copper nanoparticles. J Anal Test. 2022;6(1):3–11. https://doi.org/10.1007/s41664-022-00210-6.
39. Huang S, Guo M, Tan J, Geng Y, Wu J, Tang Y, et al. Novel fluorescence sensor based on all-inorganic perovskite quantum dots

coated with molecularly imprinted polymers for highly selective and sensitive detection of omethoate. ACS Appl Mater Interfaces. 2018;10(45):39056–63. https://doi.org/10.1021/acsami.8b14472.
40. Zhao YW, Wang Y, Yang RM, Zhang H, Zhao YF, Miao XM, et al. A zero-background fluorescent aptasensor for ultrasensitive detection of pesticides based on magnetic three-dimensional DNA walker and poly(T)-templated copper nanoparticles. Sens Actuators, B. 2021;343. https://doi.org/10.1016/j.snb.2021.130172
41. Zhang QT, Yu YY, Yun XJ, Luo B, Jiang HR, Chen CZ, et al. Multicolor colorimetric sensor for detection of omethoate based on the inhibition of the enzyme-induced metallization of gold nanorods. ACS Appl Nano Mater. 2020;3(6):5212–9. https://doi.org/10.1021/acsanm.0c00641.
42. Liu DL, Li Y, Sun R, Xu JY, Chen Y, Sun CY. Colorimetric detection of organophosphorus pesticides based on the broad-spectrum aptamer. J Nanosci Nanotechnol. 2020;20(4):2114–21. https://doi.org/10.1166/jnn.2020.17358.
43. Qian ZN, Tan RJ, Zhang XY, Leng YM, Chen ZB. MnO_2 nanosheet-based colorimetric sensor array: toward identification of organophosphorus pesticides. Microchem J. 2022;181. https://doi.org/10.1016/j.microc.2022.107758
44. Xie XM, Zhou BH, Zhang YL, Zhao GZ, Zhao B. A multi-residue electrochemical biosensor based on graphene/chitosan/parathion for sensitive organophosphorus pesticides detection. Chem Phys Lett. 2021;767. https://doi.org/10.1016/j.cplett.2021.138355
45. Zhao YS, Li XL, Chen JM, Lu X, Yang YX, Song DD, et al. Porous hierarchical peony-like cobalt-based bimetallic oxides structured by ultrathin nanosheets for highly sensitive electrochemical pesticides detection. Sens Actuators, B. 2022;352. https://doi.org/10.1016/j.snb.2021.131072
46. Ding L, Hong H, Xiao L, Hu Q, Zuo Y, Hao N, et al. Nanoparticles-doped induced defective ZIF-8 as the novel cathodic luminophore for fabricating high-performance electrochemiluminescence aptasensor for detection of omethoate. Biosens Bioelectron. 2021;192: 113492. https://doi.org/10.1016/j.bios.2021.113492.